JOURNAL OF SOLID STATE CHEMISTRY **124,** 83–94 (1996)
ARTICLE NO. 0211

Composition–Valence Diagrams: A New Representation of Topotactic Reactions in Ternary Transition Metal Oxide Systems. Application to Lithium Intercalation

P. Strobel, F. Le Cras, and M. Anne

Laboratoire de Cristallographie CNRS, BP 166, 38042 Grenoble Cedex 9, France

Received March 11, 1996; accepted March 12, 1996

Topotactic reactions in Li–*M*–O systems with *M* = Mn, Ti, V, Fe are described in the framework of composition–valence diagrams, using the Li/*M* and the transition metal valence $\nu(M)$ as coordinates. We show that this representation is very convenient to depict and compare the various parameters associated with insertion/extraction reactions, i.e., the evolution of $\nu(M)$, the extent of intercalation x in Li_xMO_y, the electrochemical potentials, and the cell parameter changes. New directions are suggested for topotactic reaction in oxides, especially in titanium ones. The composition–valence diagram helped in the detection of inconsistencies in the intercalation potentials in $LiFe_5O_8$, which are corrected using new voltammetric data. We conclude that lithium intercalation in octahedral sites of iron spinel oxides occurs at constant voltage around 1.6 V, whichever the Li–Fe–O host may be.

INTRODUCTION

Low-temperature topotactic reactions (''Chimie Douce'') have resulted in major developments in the solid state chemistry of transition metal oxides. The systematic study of oxide bronzes in the period 1950–1980 paved the way to further advances in the solid state chemistry of oxides, including the systematic exploration of alkali metal intercalation using new synthetic routes such as butyl-lithium reactions or electrochemical cells (1, 2). Topotactic synthetic chemistry also gave access to new compounds, such as λ-MnO_2 (3), several new forms of TiO_2 (4, 5), and very recently CoO_2 (6), to name a few among oxides.

The understanding of stoichiometry–structure relations is critically important in this respect: consider for instance (i) the wide range of cation and oxygen vacancies accomodated in perovskite-related structures (7), (ii) the sequence of phases found in vanadium oxide bronzes $A_xV_2O_5$ with increasing x(A = alkali metal), and (iii) the versatility in cation distribution found in spinel-type oxides (the last two examples will be addressed in this paper).

Stoichiometry relations are best described using phase diagrams, and oxygen must be considered as a separate variable in the case of transition metals where oxidation states are variable. We shall show here that the classical phase diagram based on an equilateral triangle is not always the most convenient way of presenting phase relations and especially topotactic reactions in ternary systems.

The present paper describes an alternative representation of ternary oxide systems: the composition–valence diagram, which emphasizes transition metal valence and allows direct comparison of intercalation lines. The usefulness of such diagrams will be illustrated for systems Li–*M*–O with *M* = Mn, Ti, V, and Fe, and the intercalation potentials in the spinel phases formed in these systems will be discussed in more detail.

COMPOSITION, VALENCE, AND INTERCALATION IN THE Li–Mn–O SYSTEM

We shall first illustrate the composition–valence concept in the Li–Mn–O system, which has been widely studied in a search for insertion electrode materials for rechargeable lithium batteries (8). This ternary system includes a wide range of stoichiometric spinel phases $Li_\alpha Mn_{3-\alpha}O_4$ extending from Mn_3O_4 ($\alpha = 0$) to $Li_4Mn_5O_{12}$ ($\alpha = 4/3$). But it also encompasses many other spinel stoichiometries, with either cation defects, as in λ-$MnO_2 = \square Mn_2O_4$ (3) and $Li_2Mn_4O_9$ (9), or cation excess as in the intercalated materials $Li_xMn_3O_4$ and $Li_{1+x}Mn_2O_4$ (10). In the classical, triangular phase diagram (see Fig. 1 in Refs. (11) and (12), for instance), stoichiometric spinels correspond to a constant oxygen content $x(O) = 4/7$ and follow a line parallel to the Li–Mn edge (A–C–Mn_3O_4 line in Fig. 1). The manganese valence, however, is not easily detected, since isovalent lines form a beam of lines converging to the Li_2O point, while lithium intercalation follows lines converging to the Li corner (MnO_2–B–C line in Fig. 1). Consequently, the relevant part of the diagram for intercalation studies in Mn oxide spinels ($3 \leq \nu(Mn) \leq 4$) forms a rather flat surface limited by the nonparallel Mn(4+) and Mn(3+) lines (see Fig. 1).

0022-4596/96 $18.00

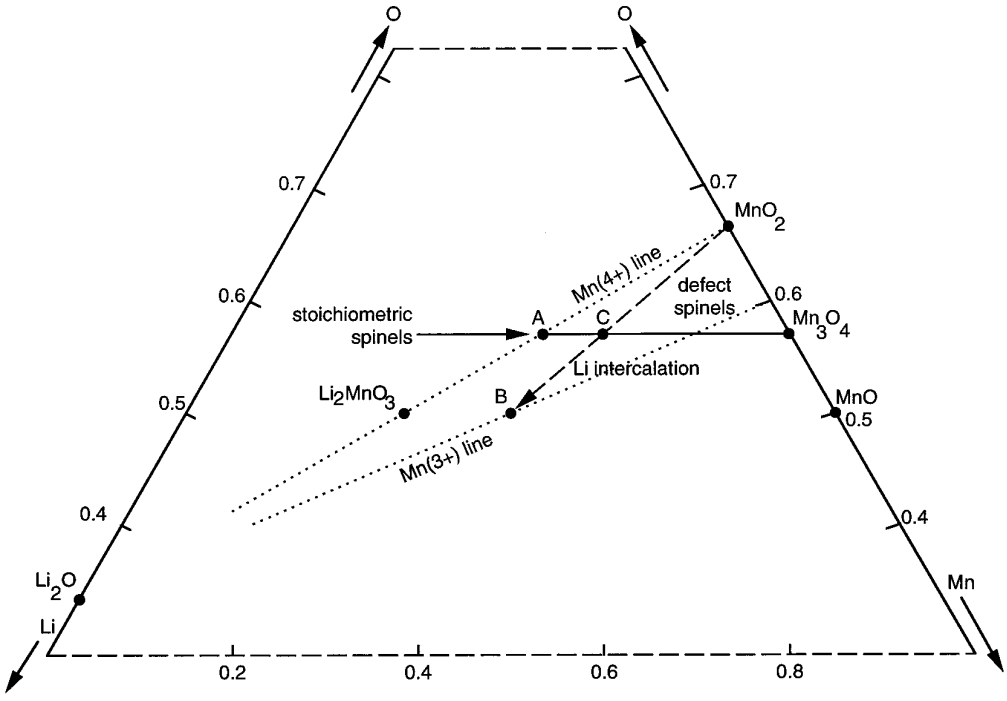

FIG. 1. Ternary phase diagram Li–Mn–O (shown for $0.3 \leq x(\mathrm{O}) \leq 0.8$).

Key experimental parameters when dealing with insertion/extraction solid state chemistry are the transition metal valence $\nu(M)$ and the guest content (x in $Li_{1+x}Mn_2O_4$, for instance), which determines the electrochemical capacity in the case of a battery. Figure 2 shows the proposed diagram for the Li–Mn–O system, using as coordinates the Li/Mn ratio and the manganese valence ν(Mn) (shown here for $0 \leq \mathrm{Li/Mn} \leq 1.3$ and $2.25 \leq \nu(\mathrm{Mn}) \leq 4$ to emphasize the spinel range). The use of coordinates related to the transition metal component instead of normalizing to $n(\mathrm{Li}) + n(\mathrm{Mn}) + n(\mathrm{O}) = 1$ changes some basic properties of the phase diagram, such as which constant quantities correspond to sets of parallel lines.

In composition–valence diagrams, it follows from our choice of axes that isovalent compositions follow horizontal, parallel lines. Two other important stoichiometric relationships are easily displayed in this kind of diagram. Constant cation/anion ratios correspond to straight lines running from top right to lower left (thick full lines in Fig. 2). These lines are no longer parallel as in Fig. 1, but they still allow one to easily distinguish stoichiometries. For spinels, the stoichiometric M_3O_4 line separates cation-defective compositions (upper left side) and intercalated ones (lower right side). In this representation, the spinel phase range forms a triangle bordered by the y-axis, the horizontal $\nu(\mathrm{Mn}) = 4$ line (top of Fig. 2), and the MO composition line. The latter two intersect at composition Li_2MnO_3, another known Li–Mn–O ternary compound with a distorted rock salt structure (13), i.e., based on the same oxygen cubic compact network as the spinels.

Consider now the general intercalation reaction

$$MO_y + x\mathrm{Li} \rightarrow \mathrm{Li}_x MO_y.$$

Since the intercalation of x Li decreases the transition metal valence from ν to $\nu - x$, the use of the Li content *with reference to the transition metal M* as the abscissa variable results in intercalation lines of constant slope -1 for intercalation of Li (or $-n$ for a guest of charge $+n$). So these form the set of parallel lines running from top left to bottom right in Fig. 2, where three known such intercalation lines are shown.

The length of the intercalation segments is directly proportional to the fraction of intercalated lithium x, hence to the theoretical capacity Q_{th} of the host material, which is related to x by the simple equation

$$Q_{\mathrm{th}} = 26800x/M_{\mathrm{o}} \qquad [\mathrm{I}]$$

with Q_{th} in mAh/g (M_{o} = molar mass of the host in g/mol).

The normalization to one transition metal atom M in the x-axis variable also simplifies capacity comparisons, unlike commonly used formulas such as Li_xMnO_2 and $Li_xMn_2O_4$, $Li_xV_2O_5$ $Li_xV_6O_{13}$, $Li_xFe_2O_3$ $Li_xFe_3O_4$, where the x values are not directly comparable due to variable transition metal stoichiometries.

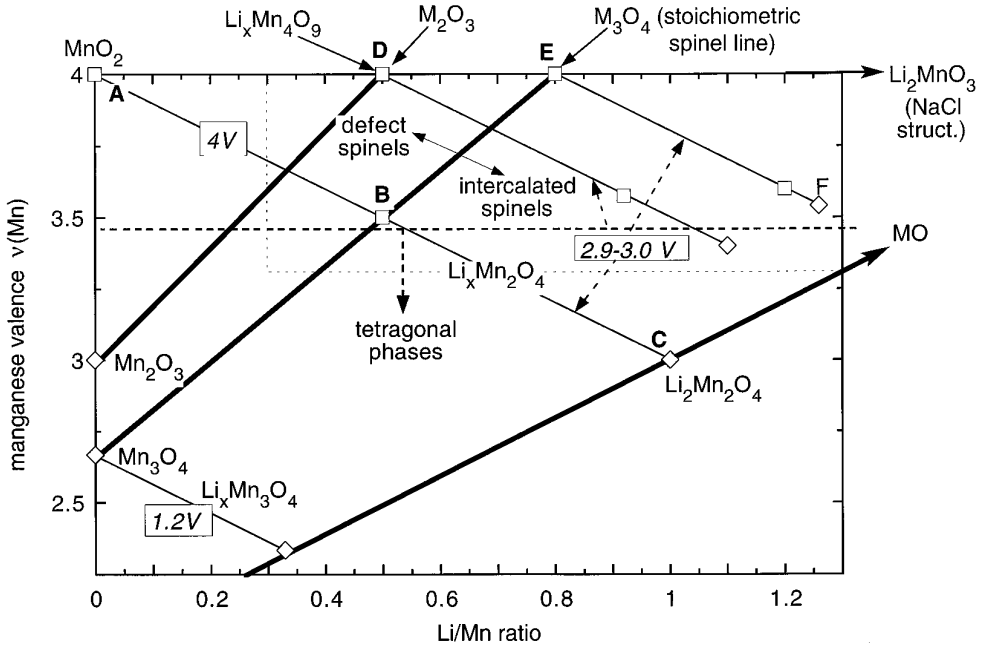

FIG. 2. Composition–valence diagram for the Li–Mn–O system. Known spinel-type compounds are shown by squares (cubic phases) or diamonds (tetragonally distorted spinels). A = λ-MnO_2, B = $LiMn_2O_4$, C = $Li_2Mn_2O_4$, D = $Li_2Mn_4O_9$, and E = $Li_4Mn_5O_{12}$. Formulas M_xO_y refer to constant overall cation/anion ratios (thick full lines). The dashed horizontal line indicates the approximate border between cubic and tetragonal phases, and the thin dashed line indicates the limits of Fig. 3.

In the Li–Mn–O system, one immediately notes the remarkable length of the $Li_xMn_2O_4$ line ABC (see Fig. 2). However, this line should actually be considered as the sum of two separate segments AB and BC, as shown by

$$\square(Mn^{+4})_2O_4 \underset{\text{Li}}{\overset{\approx 4.0\text{ V}}{\Leftrightarrow}} Li(Mn^{+3.5})_2O_4 \underset{\text{Li}}{\overset{2.95\text{ V}}{\Leftrightarrow}} Li_2(Mn^{+3})_2O_4,$$

where the reaction potentials (expressed here as cell voltages vs Li/Li^+) differ considerably between the left and right reactions.

At point C (composition $Li_2Mn_2O_4$) the overall cation/anion ration reaches 1 (*M*O line), i.e., the spinel is considered as fully intercalated (8, 11). Taking now the BC segment as a reference capacity for intercalation in the stoichiometric Li–Mn–O spinel, one notes that the length of the intercalation segments between the stoichiometric spinel line BE and the "full insertion" line *M*O increases when moving the host composition from point B toward point E. In fact, this move corresponds to the partial replacement of manganese by lighter lithium in the spinel structure, which decreases the molar mass M and hence increases the capacity Q_{th} (see Eq. [I]). This effect comes to an end at composition $Li_4Mn_5O_{12}$ (point E), which is the stoichiometric spinel with highest possible lithium content compatible with the condition $\nu(Mn) \leq 4$.

The intercalation lines are still longer if the host composition can be pushed upward from the BE line inside the BDE triangle (Fig. 2), corresponding to cation vacant compositions. A very favorable case in this respect is $Li_2Mn_4O_9$ (point D in Fig. 2). However, it has been shown that reversibility of intercalation into the defect spinel zone requires a potential in excess of 4 V (9).

Figure 2 also includes some structural information, in the form of squares or diamonds, which represent known spinel compositions with cubic or tetragonal structure, respectively. The tetrahedral distortion in manganese spinels, giving rise to the hausmannite structure, is due to the Jahn–Teller effect of the Mn^{3+} ion (electronic configuration d^4) in octahedral coordination. It is known to induce a symmetry lowering when the fraction of trivalent manganese exceeds 50% of the total manganese content (11, 14). This limit is shown in Fig. 2 (dashed horizontal line just below $\nu(Mn) = 3.5$). Note that a tetragonal composition remains above this line in Fig. 2 (point F, right side), but doubts were expressed about its exact stoichiometry in the paper reporting insertion along the EF line (11). Along the BC intercalation line, we checked by an *in situ* X-ray experiment that the tetragonal phase formation starts as soon as intercalation begins in $LiMn_2O_4$, without any detectable range of x with a variable cubic cell parameter (15).

The cubic–tetragonal phase transition is believed to be a major factor in the loss of reversible capacity observed

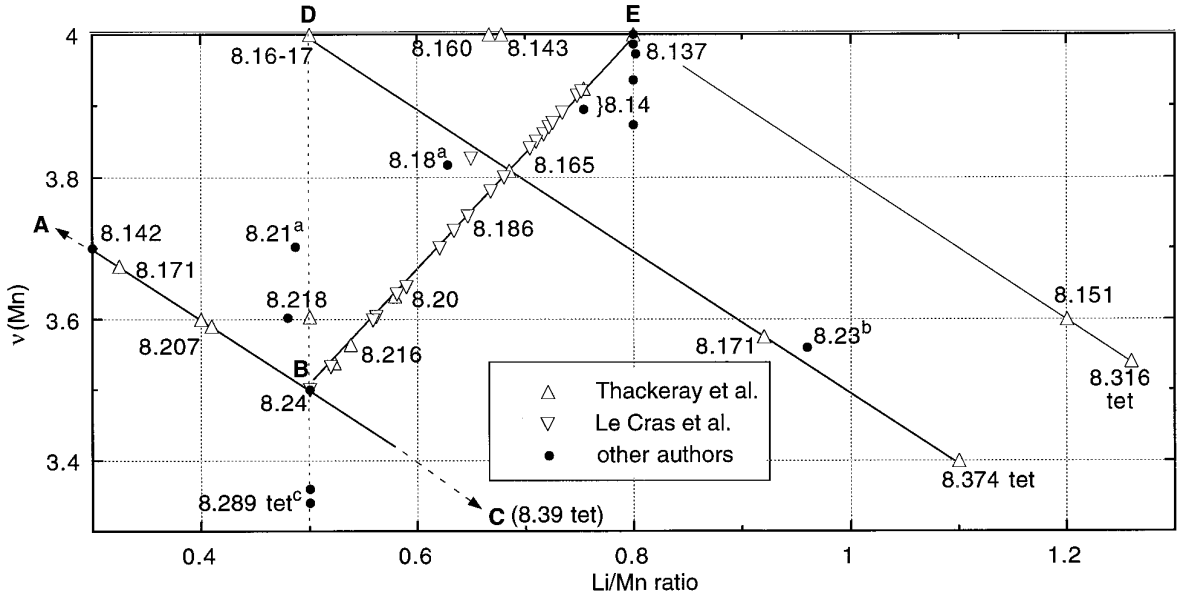

FIG. 3. Enlargement of Li–Mn–O composition–valence diagram, showing cell parameter values (in Å) vs composition for various known spinel compositions with Li/Mn ≥ 0.3. Values for tetragonal structures are the cubic root of the cell volume. [a]Feng (18), [b]Leont'eva (19), [c]Tarascon (20). Symbols A–E as in Fig. 2.

in the $Li_{1+x}Mn_2O_4$ system (11, 14). Figure 2 shows that moving the host composition toward E on the stoichiometric BE line not only increases the theoretical capacity, but also brings a larger fraction of the intercalation reaction above the cubic–tetragonal transition. However, our electrochemical tests (16) did not confirm the improvement in reversibility reported by Thackeray *et al.* (11) with initial host compositions close to $Li_4Mn_5O_{12}$. The theoretical values of total and cubic-phase intercalation capacities as a function of spinel stoichiometry have been discussed elsewhere (16).

Figure 2 also includes electrochemical reaction voltages, which can be clearly separated into three zones with very different intercalation thermodynamics:

(i) the 4 V reaction range (above the stoichiometric spinel line), corresponding to lithium insertion/extraction from tetrahedral sites;

(ii) a wide range of host compositions along the stoichiometric BE line giving rise to insertion at 2.9–3.0 V, almost irrespective of the initial stoichiometry (15, 17), and corresponding to the progressive filling of empty 16*c* octahedral sites of the spinel structure (8, 15);

(iii) a 1.2 V range for the insertion in Mn_3O_4.

Finally, one can superimpose structural data to this diagram, as shown in Fig. 3 (using average cell parameter values for tetrahedrally distorted spinels). The AB (λ-MnO_2–$LiMn_2O_4$) and BE ($LiMn_2O_4$–$Li_4Mn_5O_{12}$) lines have been well characterized (12, 14, 17, 22). The general trends are the following. The cubic cell parameter decreases with increasing manganese valence, whether this effect is produced by an increase in cation vacancies (lines BA and BD) or by an increase in Li/Mn ratio (line BE). At constant manganese valence, the Li/Mn ratio has a much smaller effect, with a maximum cell parameter value along the Li/Mn = 0.5 line. Finally, the cell volume increases on intercalation. This variation is 2.6% for the 4 V reaction AB, much more for the 3 V reactions (6.0% along BC, 8% from points D and E), with the additional drawback of the tetragonal distortion. c/a values are in the range 1.10–1.16 for the fully lithiated phases, with the highest distortion for $Li_2Mn_2O_4$, i.e., the resulting phase containing the largest fraction of Mn^{3+}.

Other topotactic reactions were reported recently in the Li–Mn–O spinel system, namely reversible exchange of *anions*. Extraction of oxygen without structural collapse was observed in Li–Mn–O spinels either by thermogravimetry at 800–1000°C (20) or by low-temperature treatment with gaseous ammonia (21).

The discussion of the Li–Mn–O composition–valence diagram focused so far on the spinel phases. Lithium insertion was also studied using as hosts other structural forms of manganese dioxide, such as β-MnO_2 (rutile-type) (23), γ-MnO_2 (24), or α-MnO_2 (hollandite-type) (25, 26). The first two structures, which contain narrow tunnels (1×1 and 1×2 MnO_6 octahedra wide, respectively) are unstable with respect to lithium insertion and transform into the spinel phase. The hollandite structure, which contains wider tunnels (2×2) usually stabilized by large cations (K, Ba, Pb, etc.), has recently been prepared with lithium

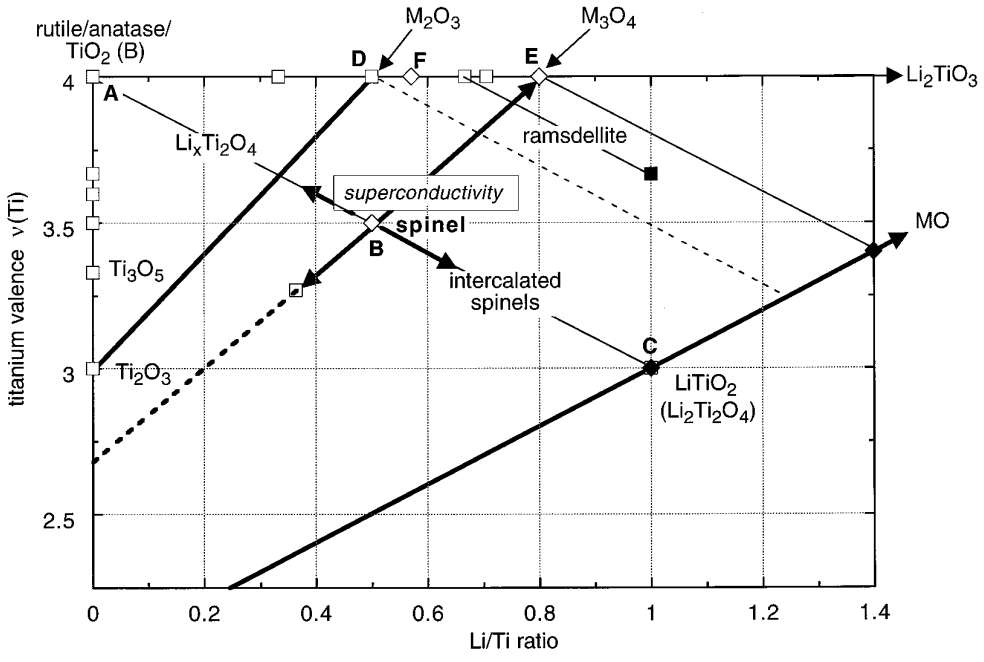

FIG. 4. Li–Ti–O composition–valence diagram. Diamonds, spinels; squares, other structures. Filled symbols, compositions achieved by lithium insertion. A = TiO_2, B = $LiTi_2O_4$, C = $Li_2Ti_2O_4$, D = $Li_2Ti_4O_9$, and E = $Li_4Ti_5O_{12}$.

as the only second cation (27, 28). ''Lithiated hollandite'' has been reported to cycle reversibly up to ca. $Li_{0.5}MnO_2$ (26), i.e., on the AB segment in Fig. 2. The reaction seems to be single-phase, with a constant decrease in voltage between 3.7 and 2.0 V. This range of potentials is markedly different from that in the spinel system cycled over the same manganese valence interval.

THE Li–Ti–O SYSTEM

This ternary system presents a number of analogies with Li–Mn–O, and also significant differences. The composition–valence diagram is shown in Fig. 4. For titanium valence $+3 \leq \nu(\mathrm{Ti}) \leq +4$, there is an extensive spinel range including $LiTi_2O_4$ and $Li_4Ti_5O_{12}$ with their intercalation lines toward the MO line. $LiTi_2O_4$ is a remarkable oxide, exhibiting superconductivity up to 13 K (29).

Few spinel compositions are known in the cation-deficient range (upper left side of the BE line). Bertaut and Durif (30) reported the vacant spinel $Li_4Ti_7O_{16}$ (point F), but the known compound $Li_2Ti_4O_9$ (point D) has a very different structure (31). Along the AB line (TiO_2–$LiTi_2O_4$), no homolog of the highly cation-deficient λ-MnO_2 is known. Attempts to extract lithium by topotactic oxidation at low temperature yielded a disordered product with broad and weak diffraction lines, corresponding to a defect rock salt structure (32). Using milder conditions, Rygula *et al.* (33), and then Capponi *et al.* on single crystals (34), found a limited nonstoichiometry range in the spinel phase (see arrow in Fig. 4). Variations in stoichiometry along either the BE or BA line are very interesting because they have a direct influence on the superconducting critical temperature T_c; this effect is illustrated for $Li_{1-x}Ti_2O_4$ in Fig. 5. The evolution of T_c along the stoichiometric $Li_{1+x}Ti_{2-x}O_4$ solid solution (BE line) has been established by several authors (29, 36).

$LiTi_2O_4$ and $Li_4Ti_5O_{12}$ spinels can be intercalated just as their manganese homologs, with a maximum capacity from point E ($Li_4Ti_5O_{12}$). The electrochemical potentials vs Li/Li^+, however, are considerably lower (≈1.5 V). The evolution of cell parameters on lithium intercalation (see

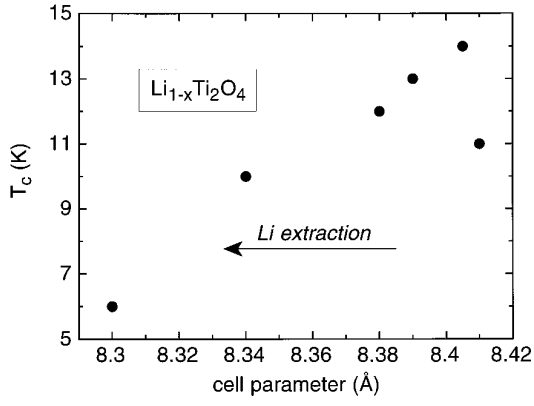

FIG. 5. Evolution of the superconducting critical temperature of $Li_{1-x}Ti_2O_4$ with cell parameters (34).

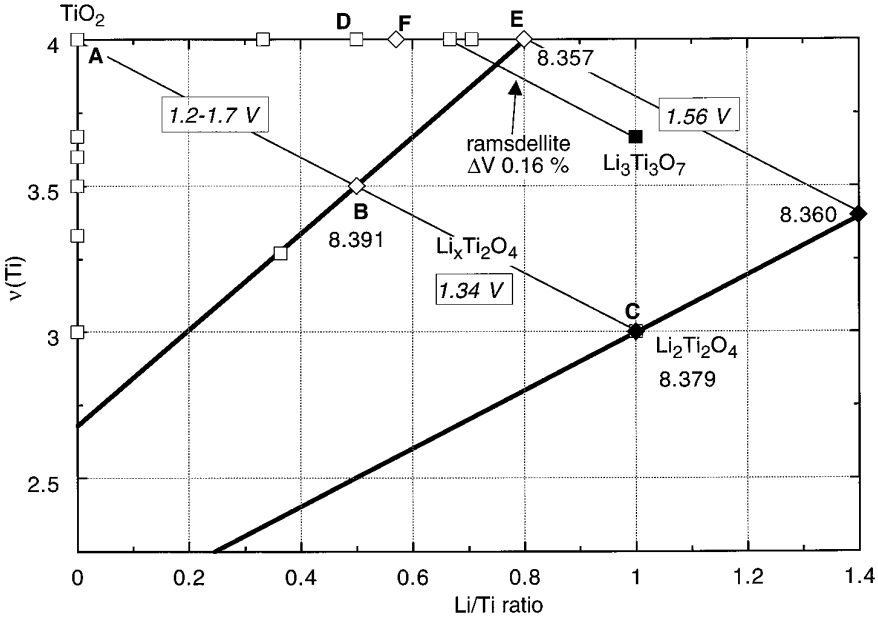

FIG. 6. Electrochemical lithium insertion voltages (vs Li/Li^+) and evolution of cell parameters (in Å) on lithium intercalation in the Li–Ti–O composition–valence diagram. Symbols A–E as in Fig. 4.

Fig. 6) shows that the Ti–O network is extremely stable, showing no distortion and a cell parameter change <0.15% for both $LiTi_2O_4$ and $Li_4Ti_5O_{12}$ hosts. Because of this remarkable invariability in unit cell size and of its low potential, $Li_4Ti_5O_{12}$ is considered as a potential anodic electrode material for Li-ion or ''rocking-chair'' batteries (36, 37).

A number of other topotactic reactions in the Li–Ti–O system are summarized in Fig. 7. The Ti^{4+} line AE includes a number of compositions with Li/Ti ratios $2/n$ (n = 3, 4, 6), which all possess monoclinic layered structures. This family of phases $A_2Ti_nO_{2n+1}$ gives rise to a rich topotactic chemistry: ion exchange between alkali cations (38) or with protons, the latter leading to the synthesis of TiO_2(B) (4). However, no lithium intercalation has been reported in these hosts to our knowledge, although they contain wide channels between the condensed Ti–O building blocks.

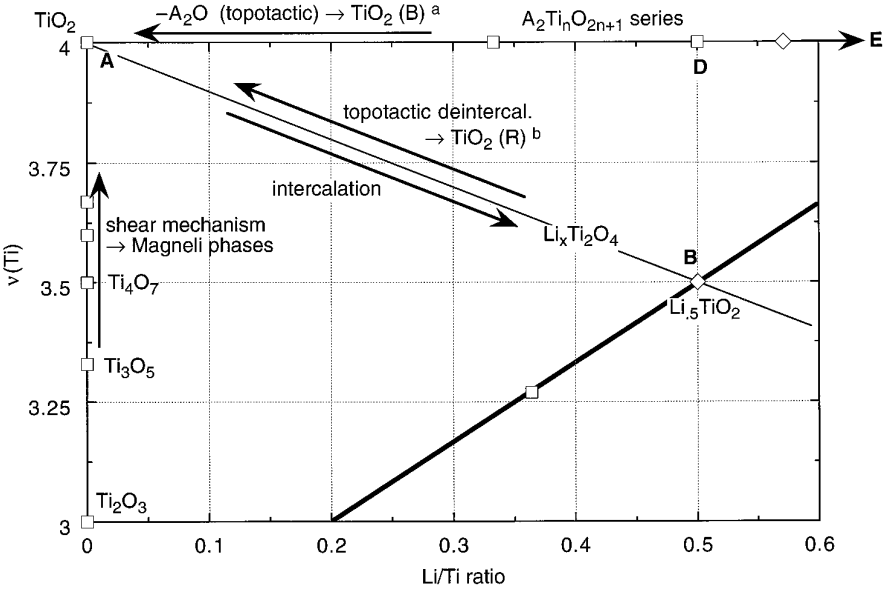

FIG. 7. Enlargement of Li–Ti–O composition–valence diagram, showing other topotactic reactions. [a]Marchand *et al.* (8), [b]Akimoto (41). Symbols A–D as in Fig. 4.

Some interesting topotactic insertion/extraction reactions have been reported in titanium oxides with the ramsdellite structure. Ramsdellite-type $Li_2Ti_3O_7$ can take up 1 Li per formula, leading to the composition $Li_3Ti_3O_7$ (39). As observed for the spinels, the variation in cell volume on lithium insertion is remarkably small (0.16%, see also Fig. 6). Note that attempts to prepare ramsdellite-type TiO_2 from $Li_2Ti_3O_7$ by a synthetic route *à la* TiO_2(B) were unsuccessful (40). Ramsdellite-type TiO_2 was finally prepared by a topotactic reaction, but by extracting lithium from ramsdellite-type $Li_{0.5}TiO_2$ (41), i.e., moving from B to A rather than from D to A in Fig. 7.

The converse reaction, lithium intercalation from TiO_2 (AB line), has been investigated in various titanium dioxide forms (32, 42). Rutile and pseudo-brookite take up only a small fraction of lithium, while anatase and TiO_2(B) intercalate lithium extensively. This difference in reactivity was ascribed to the occupation of face-sharing octahedral sites in structures with a hexagonal compact anion packing (rutile, brookite), giving rise to strong electrostatic repulsion (32). Electrochemically, the potentials vs Li/Li^+ are <2 V in all cases.

THE Li–V–O SYSTEM

This system is more complex than the Mn and Ti ones, because of the wider range of oxidation states available for the transition metal. The oxide bronze region has been described previously using triangular diagrams based on normalized atomic fractions (43–45). This portion of the Li–V–O phase diagram is shown in Fig. 8. Again, vanadium valences ν(V) and intercalation lines are not easy to depict in this representation. The very flat tetragon of interest has been distorted in (43) to make the main $Li_xV_2O_5$ intercalation line perpendicular to the Li_2O–VO_2 line.

The Li–V–O composition–valence diagram is given in Fig. 9, showing the main *chimie douce* reactions in this system. It can be conveniently divided in two main subsystems: the V_2O_5-related oxides and bronzes, i.e., starting materials with $\nu(V) > 4$, with compositions located in the upper left corner of the diagram, and the rutile-spinel group, along the A-B–$LiVO_2$ line.

(*a*) *Intercalation Hosts with* $\nu(V) > 4$ (V_2O_5, V_6O_{13}, LiV_3O_8)

The composition–valence diagram immediately shows very long intercalation lines issued from these compounds, corresponding to high theoretical electrochemical capacities. However, these lines cross several phase transitions, even at small Li/V values. In the case of V_2O_5, the successive reactions are the following:

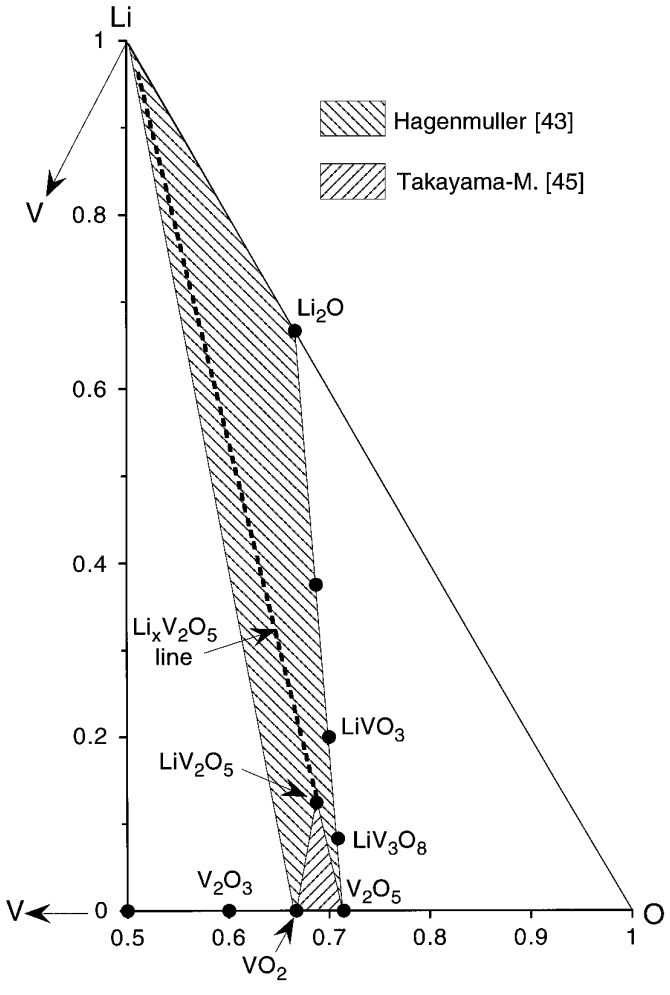

FIG. 8. Conventional Li–V–O phase diagram (only the half with O/V > 1 is shown).

$$V_2O_5 \Leftrightarrow \underset{I}{\alpha\text{-bronze}} \Leftrightarrow \underset{II}{\varepsilon\text{-bronze}} \Leftrightarrow \underset{III}{\delta\text{-bronze}} \Leftrightarrow \underset{IV}{\gamma\text{-bronze}} \Leftrightarrow \underset{V}{\omega\text{-bronze}}$$

Only the α-bronze phase, which does not extend beyond $Li/V \approx 0.05$, actually retains the V_2O_5 structure. Further intercalation alters the connecting geometry of the VO_5 coordination polyhedra and gives rise to different tunnel or layer structures (43). These first-order transitions correspond to significant jumps in potential, indicated along the intercalation lines in Fig. 10.

Reactions I, II, and III are reversible, but not reaction IV. According to Cocciantelli *et al.* (46), this is due to the formation and dissolution of VO^{2+} ions when more than one Li per V_2O_5 formula unit is inserted. Lithium insertion along the $Li_xV_2O_5$ can be pushed further, to ca. 3 Li per formula unit. The deeply discharged "bronze" with $x >\approx 1.8$ is a disordered phase called ω-V_2O_5 (47). Once formed, the γ- and ω-bronzes can be intercalated reversibly, but

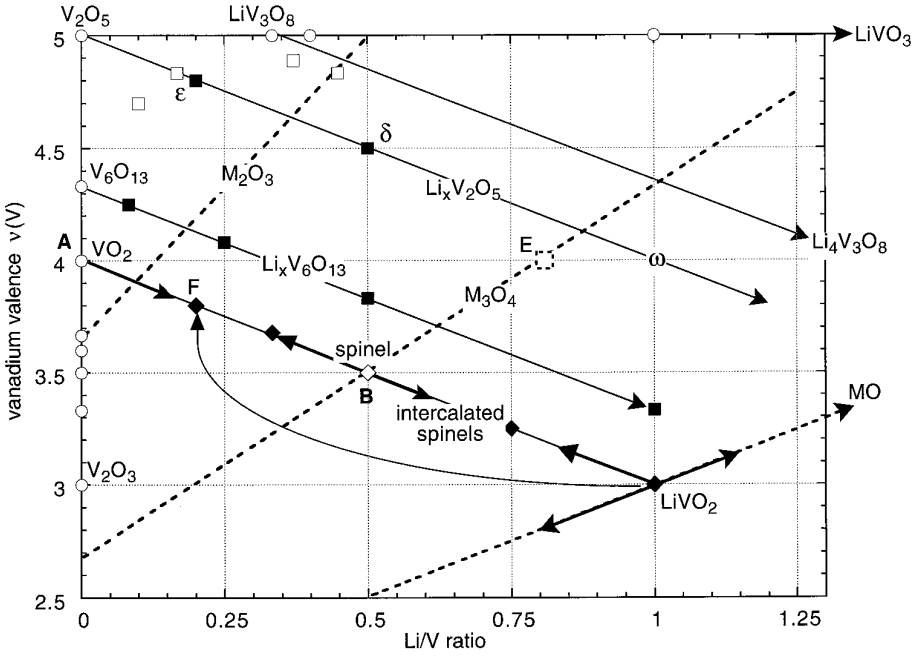

FIG. 9. Li–V–O composition–valence diagram. Squares, oxide bronzes; diamonds, spinels; circles, other stoichiometric compounds. Filled symbols, compositions achieved by lithium insertion. Some oxide bronzes are shown (greek letters). A = VO_2, B = LiV_2O_4.

follow different structural pathways giving rise to new forms of V_2O_5 (47–49).

With V_6O_{13} as a starting host, Lampe-Önnerud *et al.* (50) clearly established that the intercalation line $Li_xV_6O_{13}$ encompasses four different phases up to $Li_6V_6O_{13}$ and gives rise to as many successive voltage plateaus on the discharge curve between 3 and 1.8 V. In spite of these transitions, the reversibility seems to be good (50, 51).

$Li_xV_3O_8$, which has a different, layered structure (52), remains single-phase at least up to $x \approx 2$. The reaction is

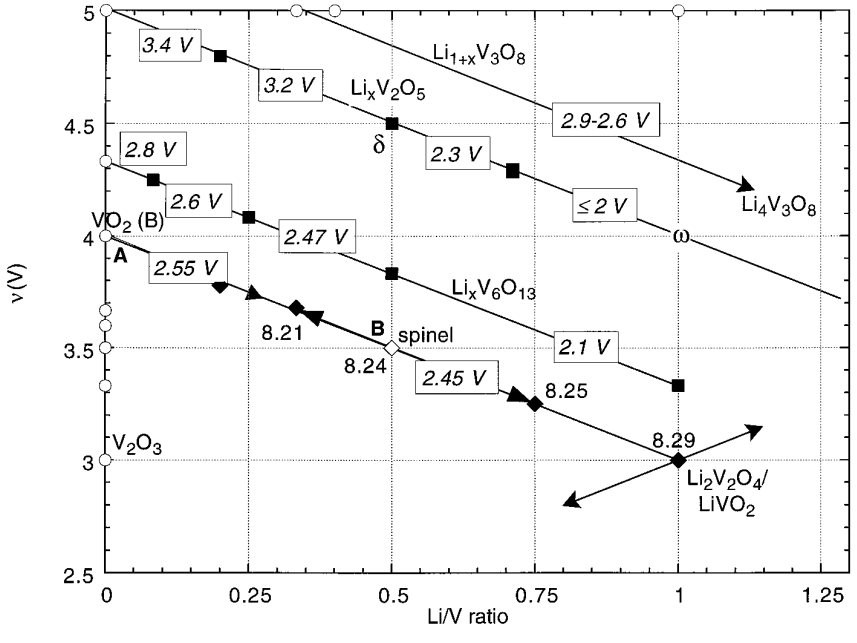

FIG. 10. Lithium intercalation voltages (vs Li/Li^+) in the Li–V–O composition–valence diagram. The spinel cell parameters (in Å) are also shown.

reversible and occurs in two steps in the potential range 2–3 V vs Li/Li^+ (53, 54). This system can intercalate lithium up to $x = 4$, but high lithium contents lead to a defect rock-salt-type structure, which accounts for a deterioration in the insertion–extraction reaction reversibility (55). Finally, note that amorphous forms of V_2O_5 and LiV_3O_8 have been prepared by low-temperature chemistry and have been shown to intercalate lithium with good reversibility (56–58).

(*b*) *The VO_2–$LiVO_2$ System*

For $3 \leq \nu(V) \leq 4$, we find analogies with the Mn and Ti systems, i.e., possible topotactic intercalation from VO_2 with MO_2(B) structure or from spinel phases centered around LiV_2O_4. Note, however, the absence of a vanadium analog of the $Li_4M_5O_{12}$ spinels known in the Mn and Ti systems. Such a composition (point E in Fig. 9) would lie close to the $Li_xV_2O_5 = Li_xV_5O_{12.5}$ intercalation line. In the vanadium system, this line encompasses two-dimensional or one-dimensional tunnel structures, but no known compositions with a 3-D network such as that in spinels. In fact, the extent of spinel solid solution $Li_\alpha V_{3-\alpha}O_4$ has not been established so far, to our knowledge.

Lithium intercalation in VO_2(B) leads to a $Li_{0.5}VO_2$ phase retaining a MO2(B)-type structure. However, it is clearly a two-phase reaction occuring at 2.55 V vs Li/Li^+ (59). Just as in the manganese case, topotactic reactions of the spinel phase LiV_2O_4 with lithium have been carried out in both insertion and extraction directions, yielding $Li_2V_2O_4$ and $Li_{\approx 0.22}VO_2$, respectively (60). In both cases, beyond a critical x value in the range 0.33–0.50 in $Li_{1\pm x}V_2O_4$, the spinel structure is not longer stable and the vanadium cations rearrange to yield other structural types (60).

Finally, in the vanadium system, even the α-$NaFeO_2$-type phase $LiVO_2$ gives rise to interesting stoichiometric variations. It gives rise to a noticeable solid solution range along the MO line (61) (see arrows in Fig. 9). Lithium can been easily extracted from it to very low lithium contents (62, 63). Interestingly, lithium extraction from either $LiVO_2$ or the LiV_2O_4 spinel yield the same trigonal compound $Li_{\approx 0.2}$ VO_2 (point F in Fig. 9), after structural rearrangement in the spinel case. All these reactions are indicated by arrows in Fig. 9.

Intercalation potentials ΔE are summarized in Fig. 10. Only the initial part of the $Li_xV_2O_5$ line (from V_2O_5 to the δ-bronze) occurs above 3 V; the absence of such a potential range on the $Li_{1+x}V_3O_8$ line shows that the vanadium valence is not the only parameter in determining ΔE. The first, short step is at 2.8–2.9 V on the $Li_xV_6O_{13}$ and $Li_{1+x}V_3O_8$ lines. The diagram then shows a wide zone of lithium insertion at 2.6–2.3 V on all intercalation lines. Its extent, however, is much larger in $Li_{1+x}V_3O_8$ and the spinel than in $Li_xV_6O_{13}$ and $Li_xV_2O_5$. The latter two can intercalate further, but at less than 2.1 V. Interestingly, these potential values depend little on the state of order of the hosts (crystallized vs sol–gel, amorphous phases). On the other hand, the potential zones thus defined are not determined by any single parameter such as the vanadium valence or Li content.

The effect of lithium insertion/extraction on the size of the spinel unit cell is also shown in Fig. 10. It expands on Li insertion, but to a lesser extent than $LiMn_2O_4$ (compare cell parameter values in Figs. 3 and 10).

THE Li–Fe–O SYSTEM

This system is much simpler, because only iron valences $+2 \leq \nu(Fe) \leq +3$ are involved in known topotactic reactions. The main compounds in this system are indicated in Fig. 11. The system is again dominated by the spinel phases, which include a solid solution $Li_\alpha Fe_{3-\alpha}O_4$ with $0 < \alpha < 0.5$ as well as the γ-form of $Fe_2O_3 = Fe[Fe_{5/3}\square_{1/3}]O_4$, with octahedral cation vacancies. The three spinels Fe_3O_4, $LiFe_5O_8$, and γ-Fe_2O_3 give rise to lithium insertion reactions, as shown in Fig. 11 (64–67).

The cell parameter values show that the cell expansion on lithium insertion is remarkably small: +2.41, +3.01, and +2.33% for Fe_3O_4, γ-Fe_2O_3, and $LiFe_5O_8$, respectively. These systems exhibit intermediate behavior between titanium and manganese spinels in this respect.

Figure 11 also displays reaction potentials. In the case of γ-Fe_2O_3, electrochemical intercalation was carried out *in situ* on a X-ray diffractometer, as well as under potentiostatically controlled discharge (66). These experiments (see Fig. 12) unambiguously showed a succession of three separate reactions as follows:

(i) Up to $Li/Fe \approx 0.15$, filling of octahedral 16*c* vacancies (potential: 2.1 V vs Li/Li^+).

(ii) A two-phase reaction at 1.60 V starting at $Li_{\approx 0.4}Fe_2O_3$, corresponding to the transformation of a spinel-type into a rock-salt-type structure (potential: 1.60 V).

(iii) A single-phase reaction at 1.4–1.2 V up to $LiFe_2O_3$, corresponding to the completion of the occupation of the rock salt octahedral sites.

In the case of $LiFe_5O_8$, previous investigations led to unconsistent results, with reported discharge curves showing either a long flat plateau at 2.1 V (64) or a continuously decreasing open-circuit potential in the range 1.7–1.2 V (65). We recently reinvestigated this system in slow-scanning potentiostatic mode (68). The results (see Fig. 12) show that the intercalation proceeds in two distinct reactions beginning at 1.7 and 1.3 V, respectively. Only the former is reversible. Figure 12 clearly shows the absence of any feature at 2.1 V comparable to the intercalation step in the vacant cationic sites observed in γ-Fe_2O_3, while

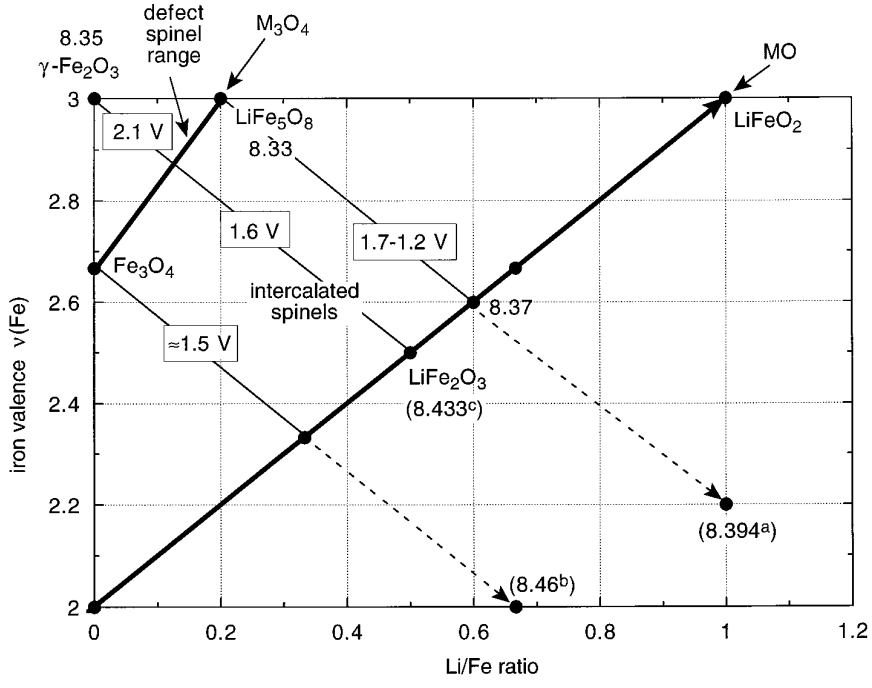

FIG. 11. Li–Fe–O composition–valence diagram. Values of cell parameters from [a]Ref. (64), [b]Ref. (65), [c]Ref. (66).

the 1.6–1.7 V step is found in both host compounds. These results confirm those of de Picciotto *et al.* (65), with the additional information that the insertion process in Li Fe_5O_8 is split into two separate reactions, detected by slow potentiostatically controlled reduction.

The intercalation voltages are indicated in the composition–valence diagram (Fig. 11), showing that the intercalation in 16*c* octahedral sites (between M_3O_4 and *M*O lines) consistently occurs at potentials 1.5–1.7 V vs Li/Li^+, whichever the M_3O_4 iron spinel host may be. The ordering of octahedral Li and Fe atoms in $LiFe_5O_8$ (space group $P4_132_2$ instead of $Fd3m$) does not seem to affect significantly the intercalation potential.

Lithium intercalaton in these systems (chemical as well as electrochemical) can been pushed farther than the theoretical structural limit (Li + Fe)/O = 1 (corresponding to complete occupation of 16*c* and 16*d* octahedral sites). As expected, such reactions, which occur below ≈1.3 V, are no longer topotactic and induce much stronger structural changes, although the cubic network seems to be maintained (65, 69). The original structure is not restored on lithium extraction.

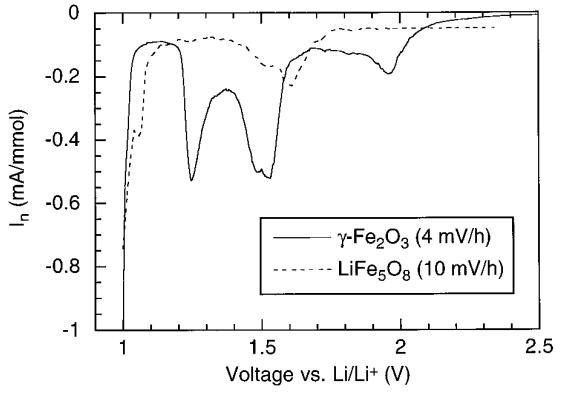

FIG. 12. Slow-scanning voltammograms of lithium cells with γ-Fe_2O_3 (66) and $LiFe_5O_8$ (68) as positive electrode.

CONCLUSIONS

The use of composition–valence diagrams is very convenient for estimating and comparing the capacities associated with intercalation reactions. In the case of the Li–Fe–O system, it helped in the detection of questionable intercalation potentials. In the Li–Mn–O system, it provides a useful coordinate system to show trends in the evolution of cell parameters in a wide solid solution region (see Fig. 3).

In addition, a comparison of composition–valence diagrams for various transition metals can give hints for topotactic reactions known to occur in a given system, which might deserve more investigations in others. Examples are:

(i) The delithiation of spinels, leading to λ-MnO_2; this remains a unique case of spinel oxide with completely

vacant tetrahedral sites. This possibility was investigated without success in the titanium system. Other transition metals might be investigated from this point of view.

(ii) Ion exchange and extraction reactions in ramsdellite-type oxides. The preparation of synthetic ramsdellite MnO_2 remains a challenge (70, 71); electrochemical intercalation attempts in this host are unsatisfactory for lithium (72, 73), and still difficult to understand for protons (71). Yet ramsdellite-type compounds gave very interesting reactions in the titanium system: lithium insertion and/or extraction, as well as ion exchange (38–41).

As a historical note, it should be noted that Brenet and co-workers introduced some 30 years ago a description of the Mn–O–H system which already showed the main characteristics of the composition–valence diagrams (74). At that time, no connection with intercalation chemistry was made, but the topotactic character of the system $Mn(OH)_2$–MnOOH–MnO_2 was already singled out.

Finally, let us point out one deficiency of composition–valence diagrams. These are constructed solely on the basis of stoichiometric parameters (cation ratio and transition metal valence), and therefore cannot make any distinction between polymorphs of similar composition. However, most reactions discussed here are topotactic, i.e., largely governed by structural considerations. In the Li–Ti–O system for instance, we discuss three very distinct topotactic reactions, all falling on the same AB line: (i) lithium extraction from spinel-type $LiTi_2O_4$, (ii) lithium insertion in various TiO_2 forms, and (iii) lithium extraction from ramsdellite-type $Li_{0.5}TiO_2$ (stoichiometrically = $LiTi_2O_4$).

This mainly shows the limits of a 2-D representation, and mostly regards the manganese and titanium dioxides, which possess dioxides with an especially complex crystal chemistry. In any case, within the composition range of a given structural type, the superimposition of crystallographic data to the stoichiometric data, as in Fig. 3, is a powerful tool for crystal chemistry analysis.

ACKNOWLEDGMENTS

We thank M. Pernet and D. Bloch for their interest in this work and stimulating discussions. F.L.C. is funded by a grant supplied by Commissariat à l'Energie Atomique and by Bolloré Technologies.

REFERENCES

1. M. B. Dines, *Mater. Res. Bull.* **10,** 287 (1975).
2. D. W. Murphy and P. A. Christian, *Science* **205,** 651 (1979).
3. J. C. Hunter, *J. Solid State Chem.* **39,** 142 (1981).
4. R. Marchand, L. Brohan, and M. Tournoux, *Mater. Res. Bull.* **15,** 1129 (1980).
5. J. Akimoto, Y. Gotoh, Y. Oosawa, N. Nonose, T. Kumagai, K. Aoki, and H. Takei, *J. Solid State Chem.* **113,** 27 (1994).
6. G. G. Amatucci, J. M. Tarascon, and L. C. Klein, *J. Electrochem. Soc.* **143,** 1114 (1996).
7. C. N. R. Rao, J. Gopalakrishnan, and K. Vidyasagar, *Indian J. Chem. A* **23,** 265 (1984).
8. M. M. Thackeray, Prog. *Batt. Batt. Mater.* **11,** 150 (1992); M. M. Thackeray, M. H. Rossouw, A. De Kock, A. De La Harpe, R. J. Gummow, K. Pearce, and D. Liles, *J. Power Sources* **43,** 289 (1993).
9. A. De Kock, M. H. Rossouw, LA. De Picciotto, M. M. Thackeray, W. I. F. David, and R. M. Ibberson, *Mater. Res. Bull.* **25,** 657 (1990).
10. M. M. Thackeray, W. I. F. David, P. G. Bruce, and J. B. Goodenough, *Mater. Res. Bull.* **18,** 461 (1983).
11. M. M. Thackeray, A. De Kock, M. H. Rossouw, D. C. Liles, R. Bittihn, and D. Hoge, *J. Electrochem. Soc.* **139,** 363 (1992).
12. R. J. Gummow, A. De Kock, and M. M. Thackeray, *Solid State Ionics* **69,** 59 (1994).
13. P. Strobel and B. Lambert-Andron, *J. Solid State Chem.* **75,** 90 (1988).
14. T. Ohzuku, M. Kitagawa, and T. Hirai, *J. Electrochem. Soc.* **137,** 769 (1990).
15. F. Le Cras, Ph.D. Thesis, Grenoble, 1996; F. Le Cras, P. Strobel, and M. Anne, to be published.
16. F. Le Cras, D. Bloch, M. Anne, and P. Stroble, *MRS Proc.* **369,** 39 (1995).
17. F. Le Cras, D. Bloch, and P. Strobel, *J. Power Sources*, in press (1996).
18. Q. Feng, Y. Miyai, H. Kanoh, and K. Ooi, *Langmuir* **8,** 1861 (1992).
19. G. V. Leont'eva, *Russ. J. Inorg. Chem.* **33,** 1254 (1988).
20. J. M. Tarascon, W. R. Mckinnon, F. Coowar, T. N. Bowmer, G. Amatucci, and D. Guyomard, *J. Electrochem. Soc.* **141,** 1421 (1994).
21. M. N. Richard, E. W. Fuller, and J. R. Dahn, *Solid State Ionics* **73,** 81 (1994).
22. M. M. Thackeray, P. J. Johnson, L. A. De Picciotto, P. G. Bruce, and J. B. Goodenough, *Mater. Res. Bull.* **19,** 179 (1984).
23. D. W. Murphy, F. J. Di Salvo, J. N. Carides, and J. V. Waszczak, *Mater. Res. Bull.* **13,** 1395 (1978).
24. T. Ohzuku, M. Kitagawa, and T. Hirai, *J. Electrochem. Soc.* **136,** 3169 (1989).
25. T. Ohzuku, M. Kitagawa, K. Sawai, and T. Hirai, *J. Electrochem. Soc.* **138,** 360 (1991).
26. M. A. Humbert, P. Biensan, M. Broussely, A. Lecerf, A. Dollé, and H. Ladhily, *J. Power Sources* **44,** 681 (1993).
27. A. Lecerf, F. Lubin, and M. Broussely, European Patent 0 386 692; U.S. Patent 4 975 346 (1990).
28. M. H. Rossouw, D. C. Liles, M. M. Thackeray, W. I. F. David, and S. Hull, *Mater. Res. Bull.* **27,** 221 (1992).
29. D. C. Johnston, *J. Low-Temp. Phys.* **25,** 145 (1976).
30. E. F. Bertaut and A. Durif, *C. R. Acad. Sci., Ser. II* **236,** 295 (1953).
31. M. Dion and Y. Piffard, *J. Inorg. Nucl. Chem.* **40,** 917 (1978).
32. D. W. Murphy, R. J. Cava, S. M. Zahurak, and A. Santoro, *Solid State Ionics* **9/10,** 413 (1983).
33. M. Rygula, S. Kemmler-Sack, T. Nissel, and R. P. Hubner, *Ann. Phys.* **2,** 685 (1993).
34. J. J. Capponi, S. Billat, P. Bordet, B. Lambert-Andron, and B. Soulette, *Physica C* **185–189,** 2721 (1991).
35. Y. Ueda, T. Tanaka, K. Kosuge, and M. Ishikawa, *J. Solid State Chem.* **77,** 401 (1988).
36. T. Ohzuku, A. Ueda, and N. Yamamoto, *J. Electrochem. Soc.* **142,** 1431 (1995).
37. M. M. Thackeray, E. Ferg, R. J. Gummow, and A. De Kock, *MRS Proc.* **369,** 17 (1995).
38. W. A. England, J. B. Goodenough, and P. J. Wiseman, *J. Solid State Chem.* **49,** 289 (1983).
39. C. J. Chen and M. Greenblatt, *Mater. Res. Bull.* **20,** 1347 (1985).
40. A. Le Bail and J. L. Fourquet, *Mater. Res. Bull.* **27,** 75 (1992).
41. J. Akimoto, Y. Gotoh, M. Sohma, K. Kawaguchi, Y. Oosawa, and H. Takei, *J. Solid State Chem.* **110,** 150 (1994).
42. B. Zachau-Christiansen, K. West, T. Jacobsen and S. Atlung, *Solid State Ionics* **28–30,** 1176 (1988).

43. P. Hagenmuller, *in* "Comprehensive Inorganic Chemistry" (J. C. Bailar, Ed.), Vol. 4, p. 541. Pergamon Press, Oxford, 1973.
44. A. A. Fotiev, L. L. Surat, L. F. Mal'tseva, and V. L. Volkov, *Russ. J. Inorg. Chem.* **22,** 1411 (1977).
45. E. Takayama-Muromachi and K. Kato, *J. Solid State Chem.* **71,** 274 (1987).
46. J. M. Cocciantelli, M. Menetrier, C. Delmas, J. P. Doumerc, M. Pouchard, M. Broussely, and J. Labat, *Solid State Ionics* **78,** 143 (1995).
47. C. Delmas, S. Brethes, and M. Menetrier, *C. R. Acad. Sci., Ser. II* **310,** 1425 (1990).
48. J. M. Cocciantelli, M. Menetrier, C. Delmas, J. P. Doumerc, M. Pouchard, and P. Hagenmuller, *Solid State Ionics* **50,** 99 (1992).
49. C. Delmas, H. Cognac-Auradou, J. M. Cocciantelli, M. Menetrier, and J. P. Doumerc, *Solid State Ionics* **69,** 257 (1994).
50. C. Lampe-Önnerud, J. O. Thomas, M. Hardgrave, and S. Ydeandersen, *J. Electrochem. Soc.* **142,** 3648 (1995).
51. J. Barker, E. S. Saidi, and M. Y. Saidi, *Electrochim. Acta* **40,** 949 (1995).
52. A. D. Wadsley, *Acta Crystallogr.* **10,** 261 (1957).
53. G. Pistoia, S. Panero, M. Tocci, R. V. Moshtev, and V. Manev, *Solid State Ionics* **13,** 311 (1984).
54. V. Manev, A. Momchilov, A. Nassalevska, G. Pistoia, and M. Pasquali, *J. Power Sources* **54,** 501 (1995).
55. L. A. De Picciotto, K. T. Adendorff, D. C. Liles, and M. M. Thackeray, *Solid State Ionics* **62,** 297 (1993).
56. J. P. Pereira-Ramos, R. Baddour, S. Bach, and N. Baffier, *Solid State Ionics* **53–56,** 701 (1992).
57. D. B. Le, S. Passerini, A. L. Tipton, B. B. Owens, and W. H. Smyrl, *J. Electrochem. Soc.* **142,** L102 (1995).
58. G. Pistoia, M. Pasquali, G. Wang, and L. Li, *J. Electrochem. Soc.* **137,** 2365 (1990).
59. B. Zachau-Christiansen, K. West, and T. Jacobsen, *Mater. Res. Bull.* **20,** 485 (1985).
60. L. A. De Picciotto and M. M. Thackeray, *Mater. Res. Bull.* **20,** 1409 (1985).
61. K. Kobayashi, K. Kosuge, and S. Kachi, *Mater. Res. Bull.* **4,** 95 (1969).
62. K. Vidyasagar and J. Gopalakrishnan, *J. Solid State Chem.* **42,** 217 (1982).
63. L. A. De Picciotto, M. M. Thackeray, and W. I. F. David, *Mater. Res. Bull.* **19,** 1497 (1984).
64. C. J. Chen, M. Greenblatt, and J. V. Waszczak, *J. Solid State Chem.* **64,** 240 (1986).
65. L. A. De Picciotto and M. M. Thackeray, *Mater. Res. Bull.* **21,** 583 (1986).
66. M. Pernet, P. Strobel, B. Bonnet, P. Bordet, and Y. Chabre, *Solid State Ionics* **259** (1993).
67. M. M. Thackeray, W. I. F. David, and J. B. Goodenough, *Mater. Res. Bull.* **17,** 785 (1983).
68. M. Pernet and P. Strobel, *in* "Defects and Diffusion Forum" (G. E. Murch, Ed.), Vol. 73, pp. 127–128, 1996.
69. I. Horio, X. Z. Zhou, and A. H. Morrish, *J. Magn. Magn. Mater.* **118,** L279 (1993).
70. M. H. Rossouw, A. De Kock, D. C. Liles, R. J. Gummow, and M. M. Thackeray, *J. Mater. Chem.* **2,** 1211 (1992).
71. L. A. H. MacLean, J. M. Amarilla, C. Poinsignon, F. Le Cras, and P. Strobel, *J. Mater. Chem.* **5,** 1183 (1995).
72. B. Zachau-Chistiansen, K. West, T. Jacobsen, and S. Skaarup, *Solid State Ionics* **70,** 401 (1994).
73. F. Le Cras, P. Strobel, and D. Bloch, unpublished results.
74. L. Balewski, J. Brenet, G. Coeffier, and P. Lançon, *C. R. Acad. Sci.* **260,** 106 (1965).